

Geometric and Electronic Structure of $[\{\text{Cu}(\text{MeAN})\}_2(\mu\text{-}\eta^2\text{:}\eta^2\text{(O}_2^{2-}))\}]^{2+}$ with an Unusually Long O–O Bond: O–O Bond Weakening vs Activation for Reductive Cleavage

Ga Young Park,^{†,⊥} Munzarin F. Qayyum,^{‡,⊥} Julia Woertink,[‡] Keith O. Hodgson,^{‡,§} Britt Hedman,[§] Amy A. Narducci Sarjeant,[†] Edward I. Solomon,^{*,‡,§} and Kenneth D. Karlin^{*,†}

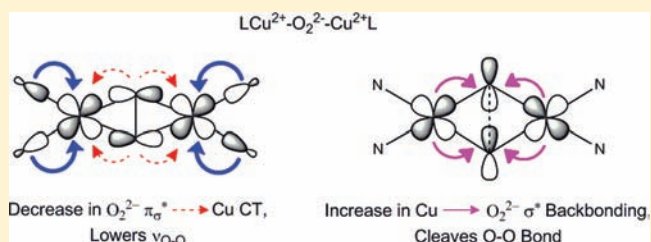
[†]Department of Chemistry, The Johns Hopkins University, Baltimore, Maryland 21218, United States

[‡]Department of Chemistry, Stanford University, Stanford, California 94305, United States

[§]Stanford Synchrotron Radiation Lightsource, SLAC, Stanford University, Menlo Park, California 94025, United States

Supporting Information

ABSTRACT: Certain side-on peroxo-dicopper(II) species with particularly low $\nu_{\text{O-O}}$ (710–730 cm^{-1}) have been found in equilibrium with their bis- μ -oxo-dicopper(III) isomer. An issue is whether such side-on peroxo bridges are further activated for O–O cleavage. In a previous study (Liang, H.-C., et al. *J. Am. Chem. Soc.* **2002**, *124*, 4170), we showed that oxygenation of the three-coordinate complex $[\text{Cu}^{\text{I}}(\text{MeAN})]^+$ (MeAN = *N*-methyl-*N,N*-bis[3-(dimethylamino)propyl]-amine) leads to a low-temperature stable $[\{\text{Cu}^{\text{II}}(\text{MeAN})\}_2(\mu\text{-}\eta^2\text{:}\eta^2\text{-O}_2^{2-})]^{2+}$ peroxo species with low $\nu_{\text{O-O}}$ (721 cm^{-1}), as characterized by UV–vis absorption and resonance Raman (rR) spectroscopies. Here, this complex has been crystallized as its SbF_6^- salt, and an X-ray structure indicates the presence of an unusually long O–O bond (1.540(5) Å) consistent with the low $\nu_{\text{O-O}}$. Extended X-ray absorption fine structure and rR spectroscopic and reactivity studies indicate the exclusive formation of $[\{\text{Cu}^{\text{II}}(\text{MeAN})\}_2(\mu\text{-}\eta^2\text{:}\eta^2\text{-O}_2^{2-})]^{2+}$ without any bis- μ -oxo-dicopper(III) isomer present. This is the first structure of a side-on peroxo-dicopper(II) species with a significantly long and weak O–O bond. DFT calculations show that the weak O–O bond results from strong σ donation from the MeAN ligand to Cu that is compensated by a decrease in the extent of peroxo to Cu charge transfer. Importantly, the weak O–O bond does not reflect an increase in backbonding into the σ^* orbital of the peroxide. Thus, although the O–O bond is unusually weak, this structure is not further activated for reductive cleavage to form a reactive bis- μ -oxo dicopper(III) species. These results highlight the necessity of understanding electronic structure changes associated with spectral changes for correlations to reactivity.



1. INTRODUCTION

In recent studies of the bioinorganic chemistry of copper, much interest has been focused on copper(I)–dioxygen adducts, due to their importance as models for copper protein O_2 -binding and activation.^{1–4} Such studies are also potentially relevant to the practical application of copper/ O_2 chemistry to synthetic oxidative transformations with organic substrates. In biochemistry, the coupled binuclear, Type 3 copper proteins include hemocyanins, tyrosinases, and catechol oxidases. In arthropods and mollusks, hemocyanins reversibly transport dioxygen. Tyrosinase functions as a catalyst for the ortho-hydroxylation of phenols to catechols and the two-electron oxidation of catechols to *o*-quinones, while catechol oxidase is responsible for the conversion of catechols to *o*-quinones.^{1,2,4,5}

In the oxy form of the active site of all of these proteins, there is a unique $\text{Cu}_2\text{-O}_2$ binding mode: a side-on $\mu\text{-}\eta^2\text{:}\eta^2$ -peroxo-dicopper(II) structure (Chart 1, middle structure) formed by one-electron transfer from each copper ion to O_2 .⁶ The first definitive X-ray characterization of such a structure occurred in a synthetic complex, where Kitajima, Fujisawa, and co-workers

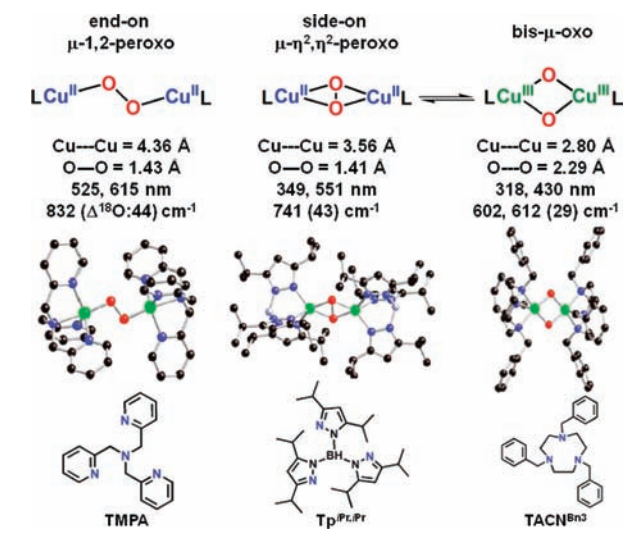
employed a highly sterically hindered diisopropyl-substituted hydrotris(pyrazolyl)borate ($\text{Tp}^{\text{iPr,iPr}}$) ligand (Chart 1 and Table 2, below).⁷ Similarities in spectroscopic and structural features known at that time for oxy-hemocyanin revealed a close match and strongly suggested the same side-on binding mode for the proteins. A subsequent X-ray structure of oxy-hemocyanin confirmed this hypothesis.⁸

While the side-on peroxo binding has been observed in copper proteins, extensive studies of biomimetic inorganic models indicate that Cu^{I} can activate O_2 and bind O_2^{2-} in several different structural modes;^{1,2,4} the particular structure obtained critically depends on the exact nature of the ligand, including its denticity and the type of donor atom (i.e., aliphatic vs aromatic N-ligand, etc.).^{1,4,9,10} One example is an end-on binding mode giving a $\text{Cu}^{\text{II}}_2(\mu\text{-}1,2\text{-}(\text{O}_2^{2-}))$ species in the now well-studied $[\{\text{Cu}^{\text{II}}(\text{TMPA})\}_2(\text{O}_2^{2-})]$ (TMPA = tris(2-pyridyl)methylamine) complex (Chart 1, left).^{11–15} These

Received: January 20, 2012

Published: May 9, 2012

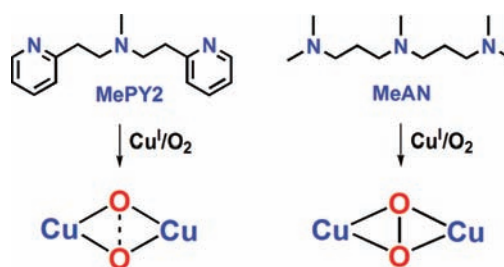
Chart 1



end-on species have $\nu_{\text{O}-\text{O}}$ around 810–850 cm^{-1} .¹ The side-on bridging mode in $\text{Cu}^{\text{II}}_2(\mu\text{-}\eta^2\text{:}\eta^2\text{-}(\text{O}_2^{2-}))$ species shows a lower $\nu_{\text{O}-\text{O}}$ of around 750 cm^{-1} . The weaker O—O bonds in side-on peroxo-bridged species have been attributed to increased π backbonding into the peroxo σ^* orbital that may result in activation of the O—O bond for reductive cleavage. A discovery by Tolman and co-workers in related $\mu\text{-}\eta^2\text{:}\eta^2$ -peroxo side-on forms demonstrated that a fully cleaved O—O bond can be generated, resulting in a new, bis- μ -oxo-dicopper(III) ($\mu\text{-O}^{2-}$)₂ species, which has now also been observed in different ligand systems (Chart 1, right), including bidentate N-donors.^{1,2,16} In the initial study¹⁷ and from subsequent investigations,^{1,2} it has been found that $\mu\text{-}\eta^2\text{:}\eta^2$ -peroxo-dicopper(II) complexes can be in rapid equilibrium with bis- μ -oxo-dicopper(III) species (Chart 1). Side-on peroxo species that also show a bis- μ -oxo component tend to have weaker O—O bonds with vibrations around 710–730 cm^{-1} , suggesting that these side-on peroxo species may be further activated for reductive cleavage. Recently, Stack and co-workers reported that phenol *o*-hydroxylation in a model system, and thus possibly in tyrosinase, could occur from a bis- μ -oxo-dicopper(III) complex, via an electrophilic mechanism.¹⁸ Chemical-spectroscopic and theoretical studies¹⁹ show that the binding of a phenolate substrate to a copper ion can lead to O—O bond cleavage in an initially formed $\mu\text{-}\eta^2\text{:}\eta^2$ -peroxo-dicopper(II) complex with $\nu_{\text{O}-\text{O}}$ of 721 cm^{-1} , generating the active $\text{Cu}^{\text{III}}_2(\text{O}^{2-})_2$ moiety.

While many synthetic systems exhibit the characteristic spectroscopic features of the side-on peroxo species, only three are crystallographically characterized (vide infra). In this report, we add a new X-ray structure to the copper–dioxygen database, the first to have a $\nu_{\text{O}-\text{O}}$ below 730 cm^{-1} . The ligand MeAN (*N*-methyl-*N,N*-bis[3-(dimethylamino)propyl]amine) and some of its solution copper(I)–dioxygen chemistry were previously described (Scheme 1).²⁰ The ligand possesses only alkyl amine N-donors.²¹ Here, its X-ray crystal structure is reported. The copper–copper separation is found to be 3.5329 (9) Å, and the O—O distance is 1.540 (5) Å. These values are out of the range of the previously structurally characterized side-on peroxo-dicopper(II) complexes. This concerned us, since we previously²² found that when $[\text{Cu}^{\text{I}}(\text{MePY2})]^+$ (MePY2 = *N*-methylbis[2-(2-pyridylethyl)]amine) reacts with O₂, a binuclear product results with an apparent long O—O distance of 1.666

Scheme 1



(12) Å.²² However, it is in fact an ~80:20 mixture of $[\{\text{Cu}^{\text{II}}(\text{MePY2})\}_2(\text{O}_2^{2-})]^{2+}$ and $[\{\text{Cu}^{\text{III}}(\text{MePY2})\}_2(\text{O}^{2-})_2]^{2+}$, as deduced from X-ray absorption spectroscopy (XAS) and resonance Raman (rR) spectroscopic studies. Thus, in this study we also probed the solid form of $[\{\text{Cu}^{\text{II}}(\text{MeAN})\}_2(\text{O}_2^{2-})]^{2+}$ using rR spectroscopy and XAS. Further, the reversible dioxygen binding and possible substrate reactivity observed for $[\{\text{Cu}^{\text{II}}(\text{MeAN})\}_2(\text{O}_2^{2-})]^{2+}$ in solution are described. Having established that this is a single $\mu\text{-}\eta^2\text{:}\eta^2$ -peroxo species, we explore why the O—O bond is particularly weak (i.e., with lengthened O—O distance and $\nu_{\text{O}-\text{O}} = 721 \text{ cm}^{-1}$) and whether it is further activated for O—O cleavage.

2. EXPERIMENTAL SECTION

General Considerations. Reagents and solvents used were of commercially available reagent quality unless otherwise stated. Methylene chloride and diethyl ether were purified by being passed through a double alumina column solvent purification system from Innovative Technologies, Inc. Acetone was distilled from Drierite under argon. Air-sensitive compounds were synthesized and handled under an argon atmosphere using standard Schlenk techniques and stored in an MBraun drybox filled with N₂. Deoxygenation of solvents was achieved either by bubbling argon through the solution for 30–45 min or by applying three freeze–pump–thaw cycles. MeAN was purchased from TCI America. $[\text{Cu}^{\text{I}}(\text{CH}_3\text{CN})_4]\text{SbF}_6$ was synthesized as previously reported.²³ Elemental analyses were performed by Desert Analytics, Tucson, AZ. The ¹H NMR spectrum was measured on a Bruker 400 MHz spectrometer, and chemical shifts are reported in ppm downfield from an internal TMS reference. Low-temperature UV–vis spectra were obtained with a Cary 50 Bio spectrophotometer equipped with a fiber-optic coupler (Varian) and a fiber-optic dip probe (Hellma 661.302-QX-UV-2 mm for low temperature). An acetone/dry ice bath (−78 °C) was used, and the temperature was monitored with a type T thermocouple thermometer (model 650, Omega Engineering, Stamford, CT). Air-sensitive solutions were prepared in a glovebox (N₂-filled, MBraun), and their reactions were carried out in custom-made Schlenk tubes designed for the dip probe (Chemglass JHU-0407-271MS). Electrospray ionization (ESI) mass spectra (Johns Hopkins University facility) were acquired using a Finnigan LCQDeca ion-trap mass spectrometer equipped with an electrospray ionization source (Thermo Finnigan, San Jose, CA). Gas chromatography (GC) experiments were carried out and recorded using a Hewlett-Packard 5890 series II gas chromatograph.

$[\text{Cu}^{\text{I}}(\text{MeAN})]\text{SbF}_6$. Under an argon atmosphere using air-free glassware, a solution of MeAN (200 mg, 1 mmol) in 10 mL of deoxygenated CH₂Cl₂ was added to solid $[\text{Cu}^{\text{I}}(\text{CH}_3\text{CN})_4]\text{SbF}_6$ (460 mg, 1 mmol). The solution was allowed to stir for 30 min at room temperature. Deoxygenated diethyl ether (60 mL) was then added with stirring at room temperature under argon until a precipitate formed. The reaction mixture was filtered under argon through a coarse-porosity frit, the solid was dried in a vacuum, and the resulting white powder was washed two times with deoxygenated diethyl ether and dried under vacuum to yield 450 mg (90%) of white solid. The product was recrystallized from CH₂Cl₂/diethyl ether. Anal. Calcd for (C₁₁H₂₇CuF₆N₃Sb): C, 26.39; H, 5.44; N, 8.39. Found: C, 26.23; H,

5.13; N, 8.32. ^1H NMR (CD_2Cl_2): δ 2.79 (bs, 4H), 2.53 (s, 16H), 2.38 (s, 3H), 1.90 (s, 2H), 1.60 (s, 2H).

[[Cu(MeAN)]₂(O₂²⁻)](SbF₆)₂. When clear acetone solutions of [Cu^I(MeAN)]SbF₆ were oxygenated at -78 °C (acetone/dry ice), intensely violet-colored solutions formed, having the characteristic spectrum of a side-on μ - η^2 : η^2 -peroxo-dicopper(II) complex, with two prominent LMCT bands, $\lambda_{\text{max}} = 360$ nm ($\epsilon = 22\,000$ cm⁻¹ M⁻¹) and 540 nm ($\epsilon = 2500$ cm⁻¹ M⁻¹). The complex precipitated as violet powder upon addition of O₂-saturated and precooled diethyl ether into the reaction mixture and was kept in a -80 °C freezer. The supernatant was decanted at -78 °C, and the resulting violet powder was washed two times with precooled diethyl ether and dried under vacuum at -78 °C. The product was recrystallized from acetone/diethyl ether in the -80 °C freezer. X-ray-quality crystals were obtained via this route.

X-ray Crystallography. X-ray crystallography was performed at the X-ray diffraction facility at Johns Hopkins University. These side-on peroxo-dicopper(II) species are typically stable only at very low temperatures. Single crystals of [[Cu(MeAN)]₂(O₂²⁻)](SbF₆)₂ were grown from an acetone solution in NMR tubes in a -80 °C freezer. Samples were kept cold during transport in a hexane/liquid N₂ bath. A low-temperature N₂ cold stream was set up over a stereomicroscope with polarizer in order to keep the crystals from decomposing during selection and mounting. In order to create the cold stream, gaseous nitrogen was passed through copper tubing submerged in liquid nitrogen; this flow was then directed onto the mounting stage of the microscope. Using Paratone oil with some of the supernatant liquid, a slurry was made in a watch glass under the microscope and cooled via the nitrogen cold stream. Crystals were then deposited in the slurry under the cold stream. A suitable crystal was selected and mounted in the slurry in a cryoloop or on the end of a glass fiber. The crystal was then held under the cold stream for several seconds to freeze it firmly in the slurry and quickly transported to the N₂ cold stream of an Oxford Diffraction Xcalibur3 diffractometer (110 K, Mo K α).

Preparation of Solid Samples for Resonance Raman and Extended X-ray Absorption Fine Structure. A recrystallized solid sample of [[Cu(MeAN)]₂(O₂²⁻)](SbF₆)₂ was prepared as describe above. Samples for rR spectra were prepared by dissolving the solid in acetone and transferring to an NMR tube using a precooled pipet. Addition of diethyl ether, standing, decantation of mother liquor, and washing/decanting with cold diethyl ether left the solid for spectroscopic analysis. Alternatively, dry cold solid was quickly transferred to a precooled NMR sample tube. For XAS samples, dry cold solid [[Cu(MeAN)]₂(O₂²⁻)](SbF₆)₂ was transferred in a similar manner to 20 mL vials.

Reversible O₂ Binding by [Cu^I(MeAN)]SbF₆. In the glovebox, [Cu^I(MeAN)]SbF₆ was dissolved in acetone, and the reaction flask was sealed with a rubber septum. Out on the benchtop, the colorless solution was bubbled with O₂ (at -78 °C), leading to the violet dioxygen adduct [[Cu(MeAN)]₂(O₂²⁻)]²⁺. Application of a vacuum while warming to -23 °C (in CCl₄ and dry ice bath) led to solution decoloration, and [Cu^I(MeAN)]SbF₆ was cleanly regenerated (O₂ dissociation as monitored by UV-vis spectroscopy). This process was repeated three times, and the cycles were monitored spectrophotometrically, leading to virtually complete overlap of all spectra; thus, there appears to be no detectable decomposition.

Solution Generation of [[Cu(MeAN)]₂(O₂²⁻)](SbF₆)₂ for Substrate Reactivity. Starting with [Cu^I(MeAN)]SbF₆, solutions of [[Cu(MeAN)]₂(O₂²⁻)]²⁺ in acetone solvent were generated as described above. An acetone solution containing 2 equiv of 2,4-di-*tert*-butylphenol was precooled and added to the [[Cu(MeAN)]₂(O₂²⁻)]²⁺ solution. The solution was left at -78 °C for 1 h. The reaction was quenched by adding 1 M HCl_(aq), and an immediate color change occurred, from violet to yellow, whereupon the solution was warmed to room temperature. After the solution was stirred for 30 min, a saturated NH₄OH/H₂O (15 mL) solution was added along with 10 mL of dichloromethane (CH₂Cl₂). The mixture was stirred for 20 min, and the CH₂Cl₂ layer was collected using a separatory funnel. The CH₂Cl₂/NH₄OH/H₂O extraction was performed three times to ensure the complete extraction of copper ion into the aqueous phase.

The CH₂Cl₂ solutions obtained were combined and dried over MgSO₄, filtered, reduced in volume by rotary evaporation, and then subjected to analysis by GC, ESI-MS, and NMR spectroscopy. Thioanisole and *N,N*-dimethylaniline were also prepared as substrates, and the reactivity was studied in a similar manner. Addition of a quenching acid solution (vide supra) was not necessary for these substrates.

Resonance Raman Spectroscopy. Resonance Raman spectra were recorded on a Princeton Instruments ST-135 back-illuminated CCD detector and on a Spex 1877 CP triple monochromator with 1200, 1800, and 2400 grooves/mm holographic spectrograph gratings. Excitation was provided by a Coherent I90C-K Kr⁺ ion laser ($\lambda_{\text{ex}} = 413.1, 568.2$ nm) or an Innova Sabre 25/7 Ar⁺ CW ion laser ($\lambda_{\text{ex}} = 379.5$ nm). The spectral resolution was <2 cm⁻¹. Spectra were recorded at powers ranging from 5 to 20 mW at the sample, and the samples were cooled to 77 K in a quartz liquid nitrogen finger Dewar (Wilmad). Baseline spectra were collected using ground, activated charcoal. Isotopic substitution was achieved by oxygenating with ¹⁸O₂ (Icon, Summit, NJ).

XAS Data Acquisition. The Cu K-edge X-ray absorption spectra of [[Cu(MeAN)]₂(O₂²⁻)](SbF₆)₂ in paste (i.e., powder with residual acetone/diethyl ether solvent) and dry powder forms were measured at the Stanford Synchrotron Radiation Lightsource (SSRL). To prevent self-absorption, the paste sample was spread in a very thin translucent layer onto a 38 μm Kapton tape applied to an aluminum window. The dry powder sample was prepared by finely grinding in boron nitride at liquid N₂ temperature to form a homogeneous mixture that was pressed into a pellet and sealed between Kapton tape windows in a 1 mm aluminum spacer. Both the powder and paste samples were prepared in a glovebag under an argon atmosphere and immediately frozen and stored under liquid N₂. All surfaces that came in contact with the sample were precooled under liquid N₂. Comparison of the extended X-ray absorption fine structure (EXAFS) and Fourier transform (FT) of the paste and the dry powder samples (Figure S3) showed no reduction in the EXAFS and FT intensity in the paste sample with respect to the dry powder, indicating the absence of any significant self-absorption in the paste sample.

XAS spectra of the paste sample were measured on the unfocused 20-pole, 2.0-T wiggler beam line 7-3. Dry powder sample data were obtained on the focused 16-pole, 2.0-T wiggler beam line 9-3. Storage ring parameters were 3 GeV and 80–100 mA. A Rh-coated pre-monochromator mirror was used for harmonic rejection and vertical collimation on both beamlines, while a cylindrical Rh-coated post-monochromator mirror was used for focusing only on beam line 9-3. A Si(220) double-crystal monochromator was used for energy selection. The samples were maintained at a constant temperature of ~ 10 K during data collection using an Oxford Instruments CF 1208 continuous-flow liquid helium cryostat. A Canberra solid-state Ge 30-element array detector was used to collect K α fluorescence for the paste, whereas transmission data were collected for the powder sample. Internal energy calibration was performed by simultaneous measurement of the absorption of a Cu foil placed between two ionization chambers located after the sample. The first inflection point of the foil spectrum was assigned to 8980.3 eV. EXAFS data are reported to $k = 12.8$ Å⁻¹ in order to avoid interference from the Zn K-edge. Photoreduction was observed for both samples, as evidenced by a gradual decrease in the energy of the edge region and slight changes in the EXAFS upon continuous scanning at the same spot. The powder data collected on BL9-3, which has a more intense beam, showed slightly more photoreduction than the paste data collected on BL7-3. To minimize effects of photoreduction, data were collected on two physically separate spots on both samples. The data reported here include an average of 12 and 3 scans for the paste and powder samples, respectively.

XAS Data Analysis. The energy-calibrated averaged data were processed by fitting a second-order polynomial to the pre-edge region and subtracting this from the entire spectrum as a background. A three-region polynomial spline of orders 2, 3, and 3 was used to model the smoothly decaying post-edge region. The data were normalized by

scaling the spline function to an edge jump of 1.0 at 9000 eV. This background subtraction and normalization was done using PySpline.²⁴ The least-squares fitting program OPT in EXAFSPAK²⁵ was used to fit the data. Initial ab initio theoretical phase and amplitude functions were generated in FEF 7.0²⁶ using crystallographic parameters of $[\{\text{Cu}(\text{MeAN})\}_2(\text{O}_2^{2-})]^{2+}$ as the starting model. Atomic coordinates were adjusted as necessary as fits were improved. During the fitting process, the bond distance (R) and the mean-square thermal and static deviations in R (σ^2) were varied for all components. The threshold energy (E_0), the point at which the photoelectron wave vector $k = 0$ was chosen as 9025 eV, was also allowed to vary for each fit but was constrained to the same value for all components in a given fit. Coordination numbers (N) were systematically varied to provide the best chemically viable agreement to the EXAFS data and their FT but was fixed within a given fit.

Computational Details. Spin-unrestricted DFT calculations were performed on $[\{\text{Cu}^{\text{II}}(\text{MeAN})\}_2(\text{O}_2^{2-})]^{2+}$ and on the structurally characterized analogue, $[\{\text{(L2)Cu}^{\text{II}}\}_2(\text{O}_2^{2-})]^{2+}$ (see Table 2), complex 1, prepared by Kodera and colleagues,²⁷ using Gaussian 03 (unless otherwise noted).²⁸ Optimizations were started from crystallographically derived parameters using the hybrid functional B3LYP (Becke GGA exchange^{29,30} with Hartree–Fock mixing and Lee, Yang, and Parr correlation^{31,32}). Calculations with BP86 functional (Becke GGA exchange with Perdew 1986 nonlocal correlation³³) incorrectly predicted the ground state of $[\{\text{Cu}^{\text{II}}(\text{MeAN})\}_2(\text{O}_2^{2-})]^{2+}$ to be a closed-shell singlet. The basis sets 6-311G* and 6-31G were used for Cu/O/N and C/H atoms respectively; this combination of Pople basis sets is referred to as B1.^{34–39} Default convergence criteria were used in all calculations unless otherwise noted. A quadratic convergence SCF procedure was employed, and structures were optimized using a density-based convergence criterion of 10^{-6} au for the SCF cycle. Optimizations using a convergence of 10^{-8} au for the SCF cycle, along with ultrafine integration grids, were also performed as checks and yielded similar geometric parameters to within 0.001 Å.

To obtain the spin-polarized broken-symmetry (BS) solutions, the two structures were first calculated with high-spin triplet states ($S_T = 1$). These high-spin wave functions were then used as initial guesses, along with the “Guess=Mix” keyword, for geometry optimizations on the BS $M_S = 0$ surface for final atomic coordinates. This resulted in spin densities of +0.452 and –0.452 on the two coppers of $[\{\text{Cu}^{\text{II}}(\text{MeAN})\}_2(\text{O}_2^{2-})]^{2+}$, with similar results for complex 1. Wave function stability calculations were performed on all optimized calculations to confirm that they corresponded to true ground states. All optimized structures were verified as minima by analytical frequency calculations that gave no imaginary frequency. The O–O stretches obtained from the frequency calculations were scaled by a factor of 0.966.⁴⁰ Optimizations were also performed with more saturated basis sets, B2 (6-311G* for Cu/O/N and 6-31G* for C/H), the Ahlrich basis sets B3 (TZVP for Cu/O/N and SVP for C/H),^{41,42} and B4 (cc-pVTZ for Cu/O/N and cc-pVDZ for C/H), with very similar findings. Calculations with B4 basis set with and without pseudopotentials on Cu (cc-pVTZ-PP) were done using Gaussian 09⁴³ with similar conclusions.

Bonding descriptions were generated by means of a Mulliken population analysis on the optimized structures. Compositions of molecular orbitals and overlap populations between molecular fragments were calculated using QMForge.⁴⁴ Each molecule was divided into three fragments (Cu_2^{4+} , O_2^{2-} , and ligand) in order to evaluate (1) the charge transfer from the ligand to the $\text{Cu}_2\text{O}_2^{2+}$ unit, (2) the backbonding from the Cu's (Cu_2^{4+}) into the peroxo (O_2^{2-}) moiety, and (3) the donation from the peroxo (O_2^{2-}) to the Cu's (Cu_2^{4+}). Orbital boundary surfaces were generated in VMD.^{45,46}

3. RESULTS AND ANALYSIS

3.1. Experimental Results. **3.1.1. X-ray Crystal Structure of $[\{\text{Cu}(\text{MeAN})\}_2(\text{O}_2^{2-})](\text{SbF}_6)_2$.** X-ray-quality crystals of $[\{\text{Cu}(\text{MeAN})\}_2(\text{O}_2^{2-})](\text{SbF}_6)_2$ were prepared as described in the Experimental Section. X-ray diffraction analysis led to the structure shown in Figure 1, with a crystallographic R -factor of

4.05%. Selected bond lengths and bond angles are listed in Table 1.

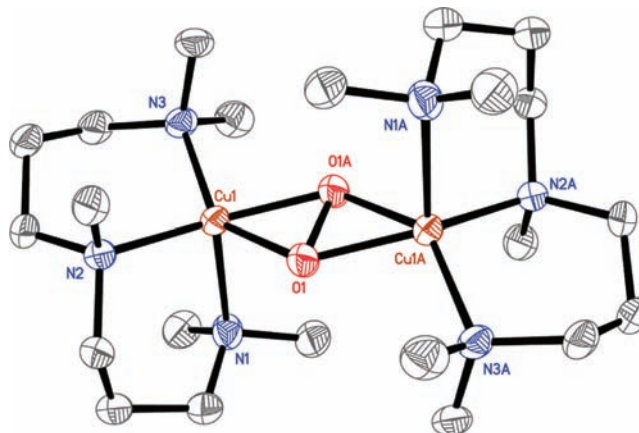


Figure 1. Displacement ellipsoid plot (50% probability level) of the cationic portion of $[\{\text{Cu}(\text{MeAN})\}_2(\text{O}_2^{2-})](\text{SbF}_6)_2$. See Table 1 for selected bond distances and angles.

Table 1. Selected Bond Distances and Angles for $[\{\text{Cu}(\text{MeAN})\}_2(\text{O}_2^{2-})](\text{SbF}_6)_2$

Cu–X	bond distance (Å)	X–Cu–X	bond angle (°)
Cu1–Cu1A	3.5329 (9)	O1A–Cu1–O1	47.11 (14)
O1–O1A	1.540 (5)	O1A–Cu1–N3	99.01 (12)
Cu1–O1A	1.919 (3)	O1–Cu1–N3	142.23 (12)
Cu1–O1	1.935 (3)	O1A–Cu1–N2	145.17 (13)
Cu1–N3	2.016 (3)	O1–Cu1–N2	102.42 (12)
Cu1–N2	2.017 (3)	N3–Cu1–N2	101.77 (13)
Cu1–N1	2.283 (3)	O1A–Cu1–N1	101.15 (12)
		O1–Cu1–N1	95.42 (12)
		N3–Cu1–N1	109.46 (13)
		N2–Cu1–N1	97.86 (13)
		O1A–O1–Cu1A	66.98 (17)
		O1A–O1–Cu1	65.91 (17)
		Cu1A–O1–Cu1	132.89 (14)

$[\{\text{Cu}(\text{MeAN})\}_2(\text{O}_2^{2-})](\text{SbF}_6)_2$ has a centrosymmetric structure (Figure 1), where each copper ion is coordinated by one MeAN ligand via the three N-donors and by the dioxygen-derived moiety, a deprotonated peroxide ligand, based on the previously published rR solution data, $\nu_{\text{O–O}} = 721$ ($\Delta^{18}\text{O}_2 = -38$).²⁰ The peroxide is bound in a $\mu\text{-}\eta^2\text{:}\eta^2$ side-on manner, bridging the copper(II) ions. Each copper(II) ion displays a slightly distorted square-pyramidal (SP) ($\tau = 0.05$; $\tau = 0.00$ for a perfect SP geometry, and $\tau = 1.00$ for a trigonal-bipyramidal structure)⁴⁷ arrangement of ligands, with the two Cu–N equatorial bonds (2.02 Å_(av)) and an elongated Cu–N axial bond (2.283(3) Å) in a trans conformation (Table 1); the peroxide ion occupies the other two equatorial positions, with Cu–O distances of 1.919(3) and 1.935(3) Å. In the X-ray structure, the resolved O–O bond distance is 1.540(5) Å, significantly longer than the O–O bond distances observed for other side-on peroxo-dicopper(II) species¹ (Table 2). Note that the O–O bond distance in hydrogen peroxide is 1.453 Å for the solid and is reported to be either 1.475 or 1.467 Å in the gas phase.⁴⁸ However, the O–O distance in $[\{\text{Cu}(\text{MeAN})\}_2(\text{O}_2^{2-})](\text{SbF}_6)_2$ is far too short for a bis- μ -oxo-dicopper(III) species, where $\text{O}\cdots\text{O} \cong 2.32$ Å.¹

Table 2. Structural/Spectroscopic Data for Structurally Characterized $\mu\text{-}\eta^2\text{:}\eta^2\text{-Peroxodicopper(II)}$ Species

	$[\text{Cu}^{\text{II}}_2(\text{L})_2(\text{O}_2^{2-})]^{2+}$ (1)	$[\{\text{Cu}^{\text{II}}(\text{L})\}_2(\text{O}_2^{2-})]^{2+}$ (2)	$[\{\text{Cu}^{\text{II}}(\text{L})\}_2(\text{O}_2^{2-})]^{2+}$ (3)	$[\{\text{Cu}^{\text{II}}(\text{L})\}_2(\text{O}_2^{2-})]^{2+}$		
	oxy-hemocyanin	oxy-tyrosinase	1 ²⁷	2 ⁷	3 ⁴⁹	MeAN
Cu...Cu (Å)	3.60 ^{a,8} , 3.54 ^b	3.55 ^{c,50}	3.523	3.560	3.519	3.533
O—O (Å)	1.41 ^{a,8} , 1.38 ^b	1.50 ^{c,50}	1.490	1.412	1.367	1.540
Cu—O av (Å)	1.98 ^{a,8} , 1.90 ^b	2.04 ^{c,50}	1.922	1.91	1.89	1.93
R-value	17.1 ⁸	21.0 ⁵⁰	5.71	10.10	5.24	4.05
UV/vis (nm)	345, 570 ⁵¹	345, 600 ⁵	366, 537	349, 551	380, 520	360, 540
rR (cm ⁻¹ ($\Delta^{18}\text{O}_2$))	744 (−39) ^{b,51}	755 (−41) ^{5,52}	765 (−41)	741 (−43)	739 (−43)	721 (−38) ²⁰
τ	0.10, 0.12 ^a ; 0.21, 0.37 ^b		0.00, 0.37	0.03, 0.03	0.29, 0.32	0.05, 0.05

^a*Limulus polyphemus*. ^b*Octopus dofleini*. ^cMushroom (*Agaricus bisporus*).

The core Cu_2O_2 structure in $[\{\text{Cu}(\text{MeAN})\}_2(\text{O}_2^{2-})](\text{SbF}_6)_2$ is compared to all known $\mu\text{-}\eta^2\text{:}\eta^2\text{-peroxo-dicopper(II)}$ structures, both protein and synthetic analogues, in Table 2. The *Limulus polyphemus* oxy-hemocyanin structure has a distorted SP geometry ($\tau = 0.10, 0.12$). The Cu...Cu and O—O distances (3.60 and 1.41 Å, respectively) are typical, but the peroxide is unsymmetrically positioned between the Cu centers. The *Octopus dofleini* oxy-hemocyanin structure possesses a 3.54 Å Cu...Cu distance and a 1.38 Å O—O bond length. However, the geometry at each Cu center is more distorted from a SP geometry ($\tau = 0.21, 0.37$), possibly due to constraints associated with the protein structure. The two protein structures of oxy-hemocyanin and one structure of oxy-tyrosinase listed in Table 2 have crystallographic R-values between 17 and 21%, indicating some disorder in the crystals. To date, there are three synthetic $\mu\text{-}\eta^2\text{:}\eta^2\text{-Cu}_2\text{O}_2$ complexes with known structures, all with $\nu_{\text{O-O}} > 730\text{ cm}^{-1}$. In $[(\text{L}2)\text{Cu}^{\text{II}}_2(\text{O}_2^{2-})]^{2+}$, complex 1 (Chart 1 and Table 2), with a binucleating L2 ligand, the metrical parameters are Cu...Cu 3.52 Å and O—O 1.49 Å (R-value 5.71%). The coordination geometry around each copper(II) center is different: one adopts a SP coordination ($\tau = 0.00$), while the other is distorted more toward a trigonal-bipyramidal geometry ($\tau = 0.37$); the authors suggested that the connectivity within the L2 ligand does not fully accommodate the Cu_2O_2 core. In the Kitajima–Fujisawa $[(\text{Tp}^{\text{iPr,iPr}})_2\text{Cu}^{\text{II}}_2(\text{O}_2^{2-})]^{2+}$ complex 2, the Cu...Cu separation is 3.56 Å and the O—O bond length is 1.41 Å (R-value 10.10%). Each Cu^{II} center is ligated in a slightly distorted SP geometry ($\tau = 0.03, 0.03$). While the quality of the structure of the side-on peroxo-dicopper(II) complex with $i\text{Pr}_3\text{tacd}$ ligands (complex 3) was marginal (R-value 5.24%),⁴⁹ a 3.52 Å Cu...Cu separation and a short O—O bond length (1.367 Å) were observed; the Cu ions in this complex have the most distorted SP geometries ($\tau = 0.29, 0.32$). Thus, the coordination geometry around each copper in $[\{\text{Cu}(\text{MeAN})\}_2(\text{O}_2^{2-})](\text{SbF}_6)_2$ is most similar to that of the pyrazolylborate ligand complex 2 and the oxy-hemocyanin structure.

There are other examples of binuclear metal complexes possessing side-on $\mu\text{-}\eta^2\text{:}\eta^2\text{-peroxo}$ bridging groups. Complexes of uranium, ytterbium, lanthanum, vanadium, rhodium, titanium, etc. can generate the side-on $\mu\text{-}\eta^2\text{:}\eta^2\text{-peroxo}$ structure. Of the examples we found,^{48,53–62} all but three have peroxo O—O bond distances shorter than 1.50 Å, the majority being between 1.45 and 1.49 Å. The O—O bond distance in $[\text{Yb}_2\{\text{N}(\text{SiMe}_3)_2\}_4(\mu\text{-}\eta^2\text{:}\eta^2\text{-O}_2)(\text{thf})_2]$ is 1.543(4) Å,⁵⁶ and exceptionally elongated bonds occur in $[\text{La}_2\{\text{N}(\text{SiMe}_3)_2\}_4(\text{O}_2)(\text{PPh}_3\text{O}_2)]$ (1.65(4) Å)⁶¹ and $[\text{Hf}(\text{TTP})_2(\text{O}_2)_2]$ (1.6 Å).⁵⁸ Of these, $\text{Yb}_2\{\text{N}(\text{SiMe}_3)_2\}_4(\mu\text{-}\eta^2\text{:}\eta^2\text{-O}_2)(\text{thf})_2$ has a reported O—O vibration;⁵⁶ its value of 775 cm^{-1} appears to be high for the reported bond length of 1.543 Å. Comparison of these peroxo lanthanide complexes to $[\{\text{Cu}(\text{MeAN})\}_2(\text{O}_2^{2-})]^{2+}$ is somewhat dubious, but such $\mu\text{-}\eta^2\text{:}\eta^2\text{-peroxo-dimetal}$ complexes do exist and indicate that, indeed, the O—O distance in $[\{\text{Cu}(\text{MeAN})\}_2(\text{O}_2^{2-})]^{2+}$ is long.

We have thus isolated and crystallographically characterized a side-on peroxo-dicopper(II) complex with an unusually long O—O bond compared to all other known protein and model side-on peroxo-dicopper(II) species. A previously reported complex, $[\{\text{Cu}^{\text{II}}(\text{MePY}2)\}_2(\text{O}_2^{2-})]^{2+}$, formed by the reaction of $[\text{Cu}^{\text{I}}(\text{MePY}2)]^+$ with O_2 , was crystallographically characterized to yield a long O—O distance of 1.666(12) Å.²² As mentioned above, however, further investigation using XAS and rR spectroscopy of both the solution- and solid-state complexes demonstrated that it in fact had an ~80:20 mixture of $[\{\text{Cu}^{\text{II}}(\text{MePY}2)\}_2(\text{O}_2^{2-})]^{2+}$ and $[\{\text{Cu}^{\text{III}}(\text{MePY}2)\}_2(\text{O}_2^{2-})_2]^{2+}$, where the side-on peroxo species has a $\nu_{\text{O-O}}$ of 729 cm^{-1} ($\Delta^{18}\text{O}_2 = -38\text{ cm}^{-1}$).²² We have, therefore, performed chemical and spectroscopic studies to investigate whether the long O—O bond in $[\{\text{Cu}(\text{MeAN})\}_2(\text{O}_2^{2-})](\text{SbF}_6)_2$ also reflects a mixture of side-on peroxo-dicopper(II) and bis- $\mu\text{-oxo-dicopper(III)}$ components.

3.1.2. Reversibility and Reactivity of $[\{\text{Cu}(\text{MeAN})\}_2(\text{O}_2^{2-})]^{2+}$. Benchtop experimental demonstration of reversible O_2 -binding would support the formation of only the side-on peroxo species, as any bis- $\mu\text{-oxo-dicopper(III)}$ isomer would lead to oxidative chemistry with solvent or ligand attack and result in

system decomposition. With that in mind, O₂ was removed by bubbling with N₂ or Ar and/or applying a vacuum and then reforming the copper–dioxygen complex by exposure to molecular dioxygen.^{63,64} The equilibrium of 2[Cu^I(MeAN)]·SbF₆ + O₂ ⇌ [{Cu(MeAN)}₂(O₂²⁻)](SbF₆)₂ is found to be cleanly reversible, as shown in Figure 2. This suggests that no bis-μ-oxo-dicopper(III) isomer formed when 2[Cu^I(MeAN)]·SbF₆ was exposed to O₂.

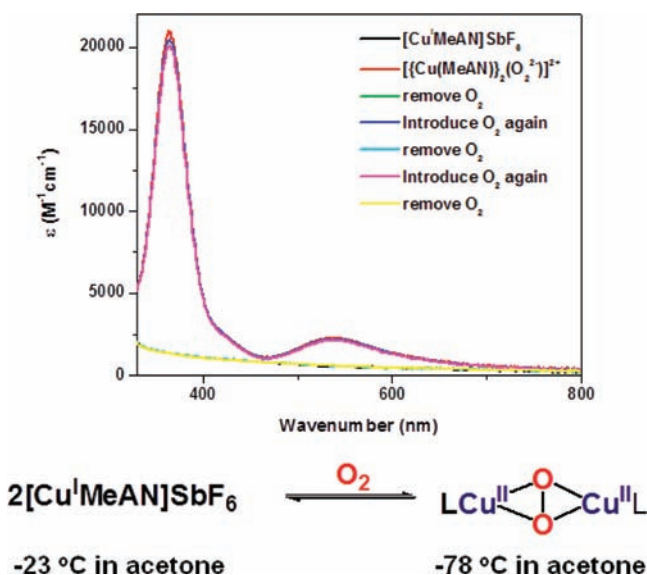
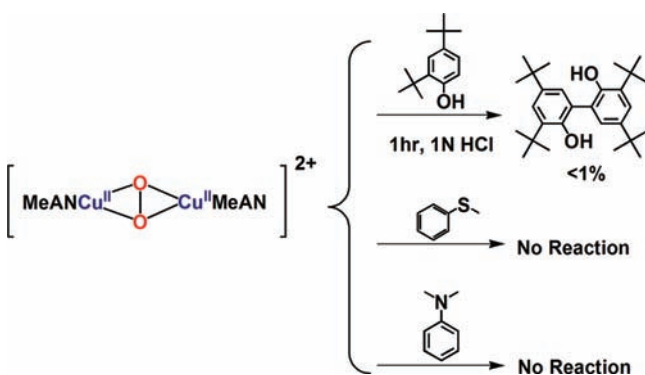


Figure 2. UV–vis spectra demonstrating the reversible O₂-binding behavior of [Cu^I(MeAN)]SbF₆ in acetone. A colorless solution of [Cu^I(MeAN)]SbF₆ spectrum (black) bubbled with O₂ (at -78 °C) leads to the violet dioxygen adduct [{Cu(MeAN)}₂(O₂²⁻)]²⁺ spectrum (red), λ_{max} = 360 nm (ε = 22 000 cm⁻¹ M⁻¹) and 540 nm (ε = 2500 cm⁻¹ M⁻¹), closely matching that known for oxyhemocyanins. Application of a vacuum while warming to -23 °C leads to solution decoloration, and [Cu^I(MeAN)]SbF₆ is cleanly regenerated. The process can be repeated many times. Here, three cycles are shown, with the dioxygen adduct spectra overlaid.

The clean, reversible dioxygen binding also implies that the peroxo complex is not capable of oxidative behavior. Indeed, [{Cu(MeAN)}₂(O₂²⁻)]²⁺ is essentially unreactive toward added substrates such as 2,4-di-*tert*-butylphenol, dimethylaniline, and thioanisole (Scheme 2). These substrates are oxidized or oxygenated by [Cu^{III}₂(μ-O)₂]²⁺ complexes, and if a bis-μ-oxo species were in equilibrium with [Cu^{II}₂(μ-η²:η²-O₂²⁻)]²⁺ in solution, such chemistry would be expected. The oxygenation

Scheme 2



product of [Cu^I(MePY2)]⁺, along with its pyridyl-substituted analogues, that had a small amount of the [Cu^{III}₂(μ-O)₂]²⁺ isomer can perform N-dealkylation chemistry and desaturation of 1,4-cyclohexadiene to benzene and of dihydroanthracene to anthracene.^{65,66} Thus, while indirect, the reversible O₂-binding behavior and lack of reactivity of [{Cu(MeAN)}₂(O₂²⁻)]²⁺ toward external substrates are consistent with the presence of only a side-on peroxo-dicopper(II) species in acetone.

3.1.3. XAS. Cu XANES. Cu K-edge XAS was performed to directly probe the oxidation state of Cu in [{Cu(MeAN)}₂(O₂²⁻)]²⁺ and quantify the presence of any bis-μ-oxo-dicopper(III) isomer. The X-ray absorption edge of [{Cu(MeAN)}₂(O₂²⁻)]²⁺ (Figure 3 left, red solid line) is characteristic of Cu^{II} and exhibits a pre-edge feature, with a maximum at ~8979.2 eV, as shown in the second-derivative plot (Figure 3, right). Conversely, bis-μ-oxo species have Cu^{III} sites which exhibit a pre-edge shift of ~1.0–2.0 eV to higher energy relative to analogous Cu^{II} complexes.⁶⁷ Figure 3 also includes edges (left) and second derivatives (right) of previously studied models, the μ-η²:η²-peroxo-dicopper(II) complex [Cu^{II}(HB(3,5-Ph₂pz)₃)₂(O₂)]⁶⁸ and the bis-μ-oxo-dicopper(III) complex [Cu^{III}₂(TACN^{Bn3})₂(O₂)]²⁺ (Chart 1).⁶⁹ Simulated edges were generated with varying ratios of these side-on peroxo and bis-μ-oxo models. The data show that [{Cu(MeAN)}₂(O₂²⁻)]²⁺ has a Cu^{II} pre-edge feature with no observable feature between 8980 and 8981 eV that would be attributed to the presence of some Cu^{III}.

Cu EXAFS. The k³-weighted EXAFS data and their FTs of [{Cu(MeAN)}₂(O₂²⁻)](SbF₆)₂ paste and powder forms are shown in Figures 4 and S1, respectively. The EXAFS fit parameters of the paste are given in Table 3. The first-shell EXAFS data were best fit with four Cu–O/N scatterers at 1.96 Å and one Cu–N/O at 2.25 Å. First-shell fits with a combination of one to three short Cu–O/N and two to four longer Cu–N/O bonds were also attempted, but these fits gave larger errors, with the split in distance between the two paths being less than the resolution of the data (0.14 Å). The EXAFS Cu–N/O vector at 2.25 Å has a high σ² relative to that obtained for the shorter Cu–O/N path, with a coordination number of four. The relatively high σ² reflects a greater disorder in this path, which is reasonable for an axial ligand. The FT peak in the R = 2.0–2.8 Å range was fit using single scattering (SS) and multiple scattering (MS) contributions from the MeAN alkyl backbone. The peak in the R = 2.8–3.8 Å range was fit with a Cu···Cu SS contribution at 3.56 Å, with its corresponding MS Cu–O–Cu vector refined to 3.65 Å when the two σ² values were linked to that of the SS path. The Cu–Cu vector is somewhat dependent on the spline functions used for data reduction (see Experimental Section), resulting in an error of ±0.04 Å. The dry powder data gave very similar results but with slightly higher σ² values, possibly because of minor decomposition product present in the sample (Table S1).

Thus, the EXAFS results indicate a side-on μ-η²:η² peroxo-dicopper(II) complex with a Cu–Cu distance of 3.56 ± 0.04 Å that is consistent with the X-ray crystallographically determined value of 3.533 Å (Table 1). The average of the four Cu–O/N bond lengths of 1.96 ± 0.02 Å also matches the average value of the X-ray crystallographically determined Cu–O and Cu–N_{eq} distances of 1.972 Å. These results suggest that only a typical side-on peroxo-dicopper(II) structure is present. In order to investigate the possibility of a small amount of bis-μ-oxo-dicopper(III) in the sample, fits were also attempted with varying ratios of ~2.8 Å Cu–Cu (typical for a bis-μ-oxo-

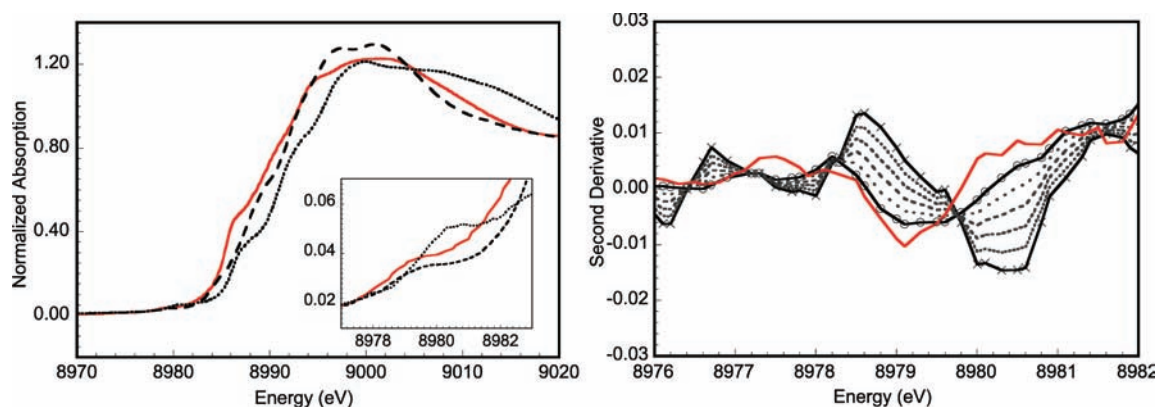


Figure 3. Comparison of the normalized Cu K-edge XAS spectra (left) and the smoothed second derivative of the pre-edge region (right) of $[\{\text{Cu}(\text{MeAN})\}_2(\text{O}_2^{2-})]^{2+}$ (red line), and the side-on $[\text{Cu}^{\text{II}}(\text{HB}(3,5\text{-Ph}_2\text{pz})_3)_2(\text{O}_2)]$ (---/○) and bis- μ -oxo $[\text{Cu}^{\text{III}}_2(\text{TACN}^{\text{Bn}3})_2(\text{O}_2)]^{2+}$ (.../×) complexes. The inset amplifies the pre-edge region. The peak at 8986.5 eV of $[\{\text{Cu}(\text{MeAN})\}_2(\text{O}_2^{2-})]^{2+}$ involves a 1s-to-4p plus a ligand-to-metal charge-transfer shakedown transition that has previously been observed in Cu^{II} complexes.⁷⁰ There is no significant Cu^{I} contamination in the sample, as shown in Figure S2 (Supporting Information). The simulated second-derivative spectra represent the following ratios of side-on to bis- μ -oxo character: 80:20, 60:40, 40:60, and 20:80 (...).

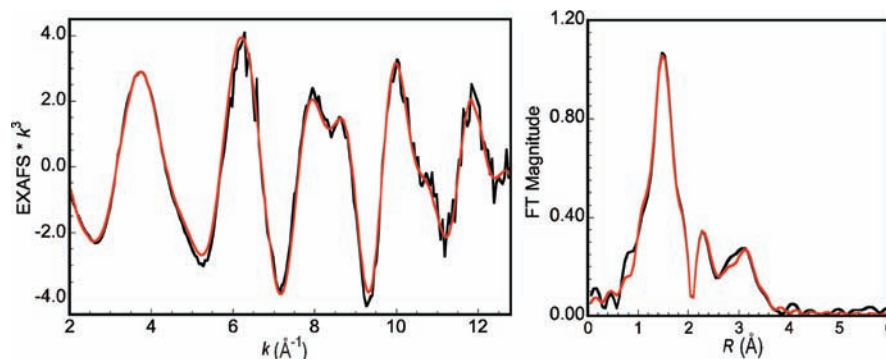


Figure 4. Cu K-edge EXAFS data and non-phase-shift-corrected Fourier transform of $[\{\text{Cu}(\text{MeAN})\}_2(\text{O}_2^{2-})](\text{SbF}_6)_2$ in the paste form. Phase shift in the first shell is ~ 0.4 Å. Data, black line; fit, red line.

Table 3. EXAFS Least-Squares Fitting Results for $k = 2\text{--}12.8$ Å^{-1} for $[\{\text{Cu}(\text{MeAN})\}_2(\text{O}_2^{2-})](\text{SbF}_6)_2$ in Paste Form

coord no./path	R (Å) ^a	σ^2 (Å ²) ^b	ΔE_0 (eV)	F^c
4 Cu–N/O	1.96	588	–9.16	0.08
1 Cu–N/O	2.25	515		
6 Cu–C	2.91	826		
12 Cu–N–C	3.14	826		
1 Cu–Cu	3.56	307		
2 Cu–O–Cu ^d	3.65	307		

^aThe estimated standard deviations in R for each fit is ± 0.02 Å. ^bThe σ^2 values are multiplied by 10^5 . ^cThe error, F , is given by $\sum[(\chi_{\text{obsd}} - \chi_{\text{calcd}})^2 k^6] / \sum[(\chi_{\text{obsd}})^2 k^6]$. ^d σ^2 for the multiple scattering path is linked to the corresponding single scattering path. The errors in ΔE_0 values are ± 0.29 eV. The estimated errors in σ^2 are 5–12%. The error in coordination number is 25%, and that in the identity of the scatterer Z is ± 1 .

dicopper(III) core) and 3.56 Å Cu–Cu pathways (typical for side-on peroxo-dicopper(II) cores) (Table S2). A very small improvement to the fit was obtained by using 0.2:0.8 mixtures of 2.76 and 3.56 Å Cu–Cu interactions. However, this improvement likely reflects the addition of two more parameters, and the Cu–Cu σ^2 for the 20% component is large (1132 Å² for 20% Cu–Cu at ~ 2.8 Å, compared to 212 Å² for 80% Cu–Cu at ~ 3.6 Å, Table 3). The fit obtained using a 0.4:0.6 mixture of ~ 2.8 to 3.56 Å Cu–Cu showed no

improvement, with the Cu–Cu σ^2 being unreasonably large (3075 Å² for 40% Cu–Cu at ~ 2.8 Å). Therefore, the EXAFS results show no evidence for a mixture containing a bis- μ -oxo isomer resulting in the long O–O bond, although a <20% contribution from a bis- μ -oxo-dicopper(III) component in the sample cannot be ruled out.

3.1.4. Resonance Raman Spectroscopy. Resonance Raman spectroscopy of the solid was performed to get a more precise upper limit on the presence of any bis- μ -oxo-dicopper(III) component. The rR spectra of solid $[\{\text{Cu}(\text{MeAN})\}_2(^{16}\text{O}_2^{2-})]^{2+}$ and $[\{\text{Cu}(\text{MeAN})\}_2(^{18}\text{O}_2^{2-})]^{2+}$ were obtained at three excitation wavelengths ($\lambda_{\text{ex}} = 568, 413, \text{ and } 380$ nm). With $\lambda_{\text{ex}} = 568$ nm excitation, an intense vibration is observed at 727 cm^{-1} , which shifts to 688 cm^{-1} upon $^{18}\text{O}_2$ substitution (Figure 5A), consistent with the $\nu_{\text{O-O}}$ of a $\mu\text{-}\eta^2\text{:}\eta^2\text{-peroxo}$ complex. Further, with $\lambda_{\text{ex}} = 380$ nm excitation, an intense $^{18}\text{O}_2$ -isotope-insensitive vibration is observed at 263 cm^{-1} , corresponding to the diagnostic Cu–Cu stretch of a $\mu\text{-}\eta^2\text{:}\eta^2\text{-peroxo}$ complex (Figure 5B). These vibrations are at energies consistent with those of the previously published MeAN side-on peroxo complex in acetone solution ($\nu_{\text{O-O}} = 721$ cm^{-1} , $\Delta^{18}\text{O}_2 = -38$ cm^{-1} , and $\nu_{\text{Cu-Cu}} = 268$ cm^{-1}). The slight difference in $\nu_{\text{O-O}}$ between the solid and solution is likely an effect of the solvent. To evaluate if any bis- μ -oxo-dicopper(III) component is present in the solid samples, rR spectra for $[\{\text{Cu}(\text{MeAN})\}_2(^{16}\text{O}_2^{2-})]^{2+}$ and $[\{\text{Cu}(\text{MeAN})\}_2(^{18}\text{O}_2^{2-})]^{2+}$ were

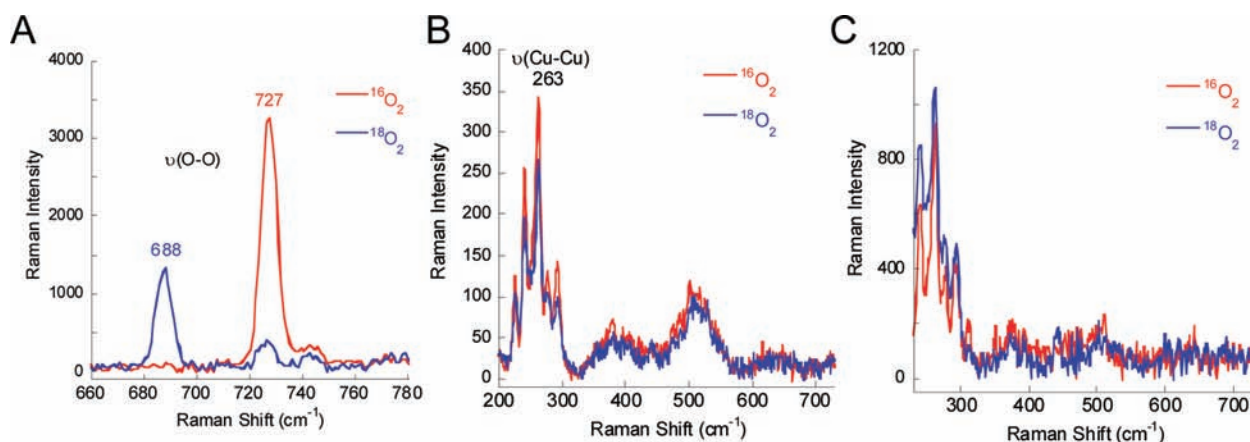


Figure 5. Resonance Raman spectra of solid $[\{\text{Cu}(\text{MeAN})\}_2(\text{O}_2^{2-})]^{2+}$ generated with $^{16}\text{O}_2$ (red) and $^{18}\text{O}_2$ (blue) with excitation wavelengths of 568 (A), 380 (B), and 413 nm (C).

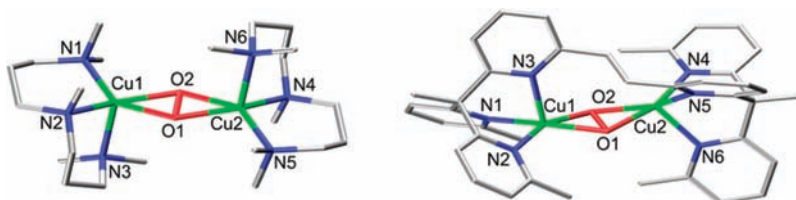


Figure 6. DFT-optimized structures of $[\{\text{Cu}^{\text{II}}(\text{MeAN})\}_2(\text{O}_2^{2-})]^{2+}$ (left) and $[(\text{L}2)\text{Cu}^{\text{II}}_2(\text{O}_2^{2-})]^{2+}$ (right) from spin-unrestricted B3LYP calculations in the BS ($M_s = 0$) state. H atoms are omitted for clarity.

obtained with $\lambda_{\text{ex}} = 413$ nm excitation, where the intense Cu–O stretch at ~ 600 cm^{-1} ($\Delta^{18}\text{O}_2 = 20\text{--}25$ cm^{-1}) of bis- μ -oxodicopper(III) complexes is most enhanced. No such vibration was observed in the rR spectrum (Figure 5C), limiting the possibility of a bis- μ -oxo-dicopper(III) isomer to less than 0.1% in the solid samples.⁷¹

Thus, the reversibility in O_2 binding and lack of reactivity of $[\{\text{Cu}(\text{MeAN})\}_2(\text{O}_2^{2-})]^{2+}$ to external substrates, coupled to spectroscopic evidence from XAS and rR, confirm that the crystallographically derived long O–O distance of 1.540 Å reflects a single species, with no bis- μ -oxo-dicopper(III) contribution. The observed $\nu_{\text{O-O}}$ for $[\{\text{Cu}(\text{MeAN})\}_2(\text{O}_2^{2-})]^{2+}$ (727 cm^{-1} in solid, 721 cm^{-1} in acetone)²⁰ is lower than for all except one other side-on $\mu\text{-}\eta^2\text{:}\eta^2$ -peroxo-dicopper(II) complex,⁷² including all the structurally characterized complexes in Table 2. The decreased $\nu_{\text{O-O}}$ observed in the MeAN complex thus reflects the unusually long peroxo O–O bond.

3.2. Calculations. **3.2.1. Correlation to Experiment.** DFT calculations were performed to investigate the origin of the long O–O bond in $[\{\text{Cu}(\text{MeAN})\}_2(\text{O}_2^{2-})]^{2+}$. Among the three other side-on peroxo-dicopper(II) complexes with known crystal structures (Table 2), complex **1**, $[(\text{L}2)\text{Cu}^{\text{II}}_2(\text{O}_2^{2-})]^{2+}$, was selected as a reference because it has the highest $\nu_{\text{O-O}}$ (765 cm^{-1} in acetone) of these structurally defined complexes.⁷³

Selected geometric parameters from the DFT-optimized structures of complex **1** and $[\{\text{Cu}^{\text{II}}(\text{MeAN})\}_2(\text{O}_2^{2-})]^{2+}$ (Figure 6) calculated using the B3LYP functional and B1 basis set are compared to those obtained from crystallography in Tables 4 and 5, respectively. Although the calculated Cu–Cu and O–O distances are characteristic of side-on peroxo complexes, the Cu–Cu distance is longer and the O–O distance is shorter in both calculated structures compared to their corresponding crystal structures. The calculated structure of **1** shows a butterfly Cu_2O_2 core that parallels the crystallographic

Table 4. Comparison of Selected Geometric Parameters of $[\{\text{Cu}^{\text{II}}(\text{L}2)\}_2(\text{O}_2^{2-})]^{2+}$ (1**) from DFT Calculations and Crystallography^a**

parameter	X-ray	DFT	DFT ^b
$\angle\text{Cu}_1\text{O}_1\text{O}_2\text{Cu}_2$	168.2°	158.7°	158.9°
$\text{Cu}_1\text{--Cu}_2$	3.523	3.597	3.591
$\text{O}_1\text{--O}_2$	1.490	1.475	1.490
$\text{Cu}_1\text{--O}_1$	1.918	1.978	1.975
$\text{Cu}_1\text{--O}_2$	1.912	1.944	1.947
$\text{Cu}_2\text{--O}_1$	1.895	1.934	1.935
$\text{Cu}_2\text{--O}_2$	1.961	2.036	2.035
$\text{Cu}_1\text{--N}_1$	1.967	2.000	1.999
$\text{Cu}_1\text{--N}_2$	1.962	1.996	1.997
$\text{Cu}_1\text{--N}_3$	2.263	2.295	2.295
$\text{Cu}_2\text{--N}_4$	1.968	1.988	1.989
$\text{Cu}_2\text{--N}_5$	2.031	2.057	2.053
$\text{Cu}_2\text{--N}_6$	2.124	2.163	2.168

^aAll bond lengths are in Å. ^bDFT^b calculation, performed by constraining O–O to 1.490 Å, increases electronic and Gibbs free energy (at 153 K) by 0.04 and 0.27 kcal/mol, respectively.

structure (Table 4, $\angle\text{CuOOCu}$). All the other geometric parameters of **1** are also in reasonable agreement with the crystal structure. For $[\{\text{Cu}^{\text{II}}(\text{MeAN})\}_2(\text{O}_2^{2-})]^{2+}$, the Cu_2O_2 core is calculated to be planar, again in agreement with the crystal structure (Table 5, $\angle\text{CuOOCu}$). The O–O bond length in $[\{\text{Cu}^{\text{II}}(\text{MeAN})\}_2(\text{O}_2^{2-})]^{2+}$ is calculated to be longer than in **1** (Table 6). Analytical frequency calculations also parallel the experimentally observed trend in $\nu_{\text{O-O}}$ and isotope shifts but yield $\nu_{\text{O-O}}$ values that are higher than the experimental ones (as often found in DFT calculations and consistent with the shorter calculated O–O distances) (Table 6).

Table 5. Comparison of Selected Geometric Parameters of $[\{\text{Cu}^{\text{II}}(\text{MeAN})\}_2(\text{O}_2^{2-})]^{2+}$ from DFT Calculations and Crystallography^a

parameter	X-ray	DFT	DFT ^b
$\angle\text{Cu}_1\text{O}_1\text{O}_2\text{Cu}_2$	180.0°	180.0°	180.0°
Cu ₁ –Cu ₂	3.533	3.676	3.650
O ₁ –O ₂	1.541	1.487	1.541
Cu ₁ –O ₁	1.934	2.001	1.998
Cu ₁ –O ₂	1.920	1.964	1.964
Cu ₂ –O ₁	1.920	1.964	1.964
Cu ₂ –O ₂	1.934	2.002	1.998
Cu ₁ –N ₁	2.017	2.041	2.043
Cu ₁ –N ₂	2.016	2.036	2.037
Cu ₁ –N ₃	2.285	2.347	2.355
Cu ₂ –N ₄	2.016	2.036	2.037
Cu ₂ –N ₅	2.017	2.041	2.043
Cu ₂ –N ₆	2.285	2.347	2.355

^aAll bond lengths are in Å. ^bDFT^c calculation, performed by constraining O–O to 1.541 Å, increases electronic energy by 0.77 kcal/mol but decreases Gibbs free energy at 110 K by 0.07 kcal/mol.

Table 6. Experimental and Calculated O–O Distances and Vibrations in $[\{\text{Cu}^{\text{II}}(\text{MeAN})\}_2(\text{O}_2^{2-})]^{2+}$ and $[(\text{L}2)\text{Cu}^{\text{II}}_2(\text{O}_2^{2-})]^{2+}$ (1**)^a**

parameter	MeAN	1	difference
O ₁ –O ₂ (exp) ^b	1.540	1.490	0.050
O ₁ –O ₂ (calc)	1.487	1.475	0.012
$\nu_{\text{O-O}}$ (exp) ^c	721 (–38)	765 (–41)	44
$\nu_{\text{O-O}}$ (calc) ^d	784 (–44)	807 (–47)	23

^aAll bond lengths and vibrations are in Å and cm^{–1}, respectively. ^b $\Delta^{18}\text{O}_2$ is reported in parentheses. ^cCrystallographically derived parameter. ^dRaman measurements were done in acetone. ^eA scaling factor of 0.966 was used on the calculated vibrations.⁴⁰

The experimental difference in O–O distance between $[\{\text{Cu}^{\text{II}}(\text{MeAN})\}_2(\text{O}_2^{2-})]^{2+}$ and **1** (Table 6) is 0.050 Å, whereas the calculated difference is smaller (0.012 Å). The 0.012 Å difference in bond length leads to a 23 cm^{–1} calculated difference in $\nu_{\text{O-O}}$ value, which is smaller than the experimentally observed frequency difference of 44 cm^{–1}.⁷⁴ When the O–O distances in $[\{\text{Cu}^{\text{II}}(\text{MeAN})\}_2(\text{O}_2^{2-})]^{2+}$ and **1** are constrained to their crystallographic values (1.541 and 1.490 Å, respectively) (Tables 4 and 5), the increase in electronic energy is only 0.77 kcal/mol for $[\{\text{Cu}^{\text{II}}(\text{MeAN})\}_2(\text{O}_2^{2-})]^{2+}$ and 0.04 kcal/mol for **1**. Thus, there is a fairly flat potential energy surface that could lead to some variability in the calculated core distances.⁷⁵

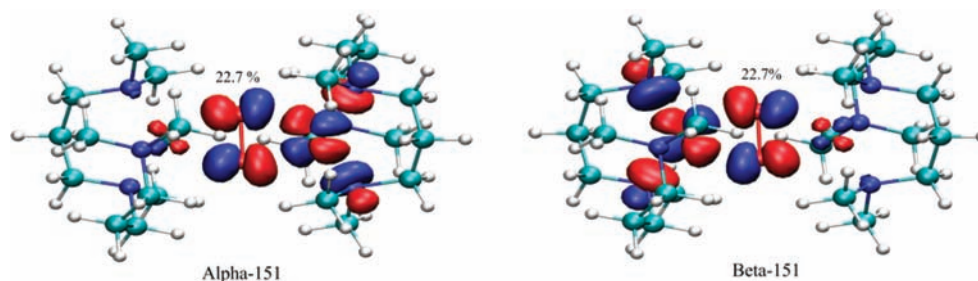
3.2.2. Bonding Description. As the DFT calculations qualitatively reproduce the longer O–O bond and the lower $\nu_{\text{O-O}}$ (Table 6) in the MeAN complex relative to **1**, we can use these calculations to gain insight into the factors that lead to this particularly weak O–O bond. Both molecules are well described as having BS singlet ($M_S = 0$) ground states, consistent with the experimentally determined diamagnetism of the side-on peroxo complexes. The α - and β -holes reside in the 3d_{xy} orbitals on each Cu (x - and y -axes are along Cu–Cu and O–O, respectively).⁷⁶ The peroxo–Cu bonding is dominated by donation from the filled $\text{O}_2^{2-} \pi^*_\sigma$ orbital (the peroxide π^* HOMO that is in the Cu_2O_2 plane and σ antibonding to Cu) into the singly occupied Cu 3d_{xy} orbitals (Figure 7). This results in 22.7% O_2^{2-} character mixed into both the α and the β Cu-based LUMOs (Table S3).⁷⁷ Given the planarity of the Cu_2O_2 core of $[\{\text{Cu}^{\text{II}}(\text{MeAN})\}_2(\text{O}_2^{2-})]^{2+}$, there is essentially no π^*_ν (the peroxide π^* HOMO perpendicular to the Cu_2O_2 plane) donor interaction between the O_2^{2-} and the Cu. In **1**, the Cu_2O_2 core is butterflyed, leading to a mixture of π^*_σ and π^*_ν donor character in the α and β unoccupied d_{xy} orbitals.

The two main contributions to the O–O stretching frequency in the Cu_2O_2 complexes are the peroxo π^*_σ donation into the Cu d_{xy} orbitals described above and the backbonding from the occupied Cu d into the unoccupied peroxo σ^* orbital. A few percent electron donation into σ^* is very efficient at lowering the O–O vibration in side-on peroxo species.^{78,79} The bonding interactions between O_2^{2-} and Cu were calculated by fragment analysis using *QMForge*.⁴⁴ The charge transfer from the $\text{O}_2^{2-} \pi^*$ orbitals into Cu, the backbonding from Cu into the $\text{O}_2^{2-} \sigma^*$, and the donation from the ligand to the Cu in MeAN and **1** are compared in Table 7 using Mulliken populations.

Table 7. Bonding and Backbonding Charge-Transfer Contributions Calculated from a Fragment Analysis of $[\{\text{Cu}^{\text{II}}(\text{MeAN})\}_2(\text{O}_2^{2-})]^{2+}$ and **1 Using Mulliken Populations**

	MeAN	1
$\sigma^*(\text{Cu} \rightarrow \text{O}_2^{2-})^a$	1.62	1.97
$\pi^*(\text{O}_2^{2-} \rightarrow \text{Cu})^b$	53.15	57.38
ligand \rightarrow Cu ^c	55.41	48.39

^aSummation of the unoccupied σ^* O_2^{2-} fragment orbital in the α and β occupied molecular orbitals. ^bSummation of the occupied π^*_σ and π^*_ν O_2^{2-} fragment orbitals in the α and β unoccupied molecular orbitals. ^cDifference between the population of the total occupied ligand orbitals from the whole molecule and the total ligand fragment occupied orbitals.

**Figure 7.** Isosurface plots (isovalue 0.04 au) of α and β LUMO of $[\{\text{Cu}^{\text{II}}(\text{MeAN})\}_2(\text{O}_2^{2-})]^{2+}$ from spin-unrestricted B3LYP calculations in the BS ($M_S = 0$) state.

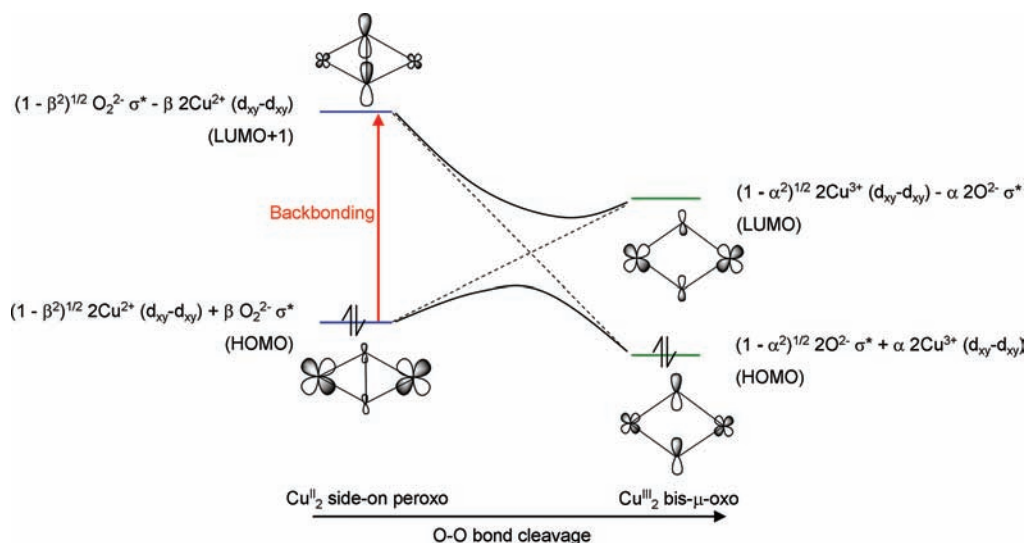


Figure 8. Side-on peroxo-dicopper(II) to bis- μ -oxo-dicopper(III) correlation diagram showing the two key molecular orbitals. An increase in O–O distance results in increased charge transfer from Cu d into $O_2^{2-} \sigma^*$ orbital (illustrated by the red arrow). Cleavage of the O–O bond oxidizes the Cu's and results in the formation of the bis- μ -oxo-dicopper(III) structure.

The fragment analysis shows that backbonding from Cu into the peroxo σ^* is greater for **1** than for $[\{Cu^{II}(MeAN)_2(O_2^{2-})\}_2]^{2+}$ (Table 7) and thus does not correlate with its experimentally observed increase in ν_{O-O} (Table 6). However, the peroxo π^* -to-Cu charge transfer does correlate with the low ν_{O-O} of $[\{Cu^{II}(MeAN)_2(O_2^{2-})\}_2]^{2+}$. The MeAN complex has less $O_2^{2-} \pi^*$ donation, and thus higher electron density in the peroxo π antibonding orbitals, resulting in the lower ν_{O-O} . Table 7 further shows that the decrease in peroxo π^* donation in $[\{Cu^{II}(MeAN)_2(O_2^{2-})\}_2]^{2+}$ is associated with an increase in the ligand donation, as the ligand is trans to the peroxo–Cu bond. A parallel trend in charge transfer is observed with the calculated structures of $[\{Cu^{II}(MeAN)_2(O_2^{2-})\}_2]^{2+}$ and **1**, where the O–O bond lengths have been constrained to the crystallographic values (Table S6).

4. DISCUSSION

An X-ray crystal structure of the binuclear copper(I)/dioxygen adduct, $[\{Cu^{II}(MeAN)_2(\mu-\eta^2:\eta^2-O_2^{2-})\}_2]^{2+}$, has been obtained that shows an unusually long O–O bond length of 1.540(5) Å, with a copper–copper distance of 3.5329(9) Å; the crystallographically derived displacement parameters are well-behaved. The results obtained from XAS and rR studies confirm that the crystalline $[\{Cu^{II}(MeAN)_2(\mu-\eta^2:\eta^2-O_2^{2-})\}_2]^{2+}$ is not a mixture of side-on peroxide dicopper(II) and bis- μ -oxo-dicopper(III) isomers. The X-ray structure, spectroscopic analysis, and solution behavior (i.e., clean reversible binding of O_2 and lack of external substrate reactivity) all show that $[\{Cu^{II}(MeAN)_2(\mu-\eta^2:\eta^2-O_2^{2-})\}_2]^{2+}$ is a pure complex. This is in contrast to the structure for MePY₂,²² where a long O–O bond in the crystal structure reflected a mixture of side-on peroxo and bis- μ -oxo components. Thus, the low ν_{O-O} experimentally observed for $[\{Cu^{II}(MeAN)_2(\mu-\eta^2:\eta^2-O_2^{2-})\}_2]^{2+}$ does, in fact, reflect a long, weak O–O bond.

Calculations show that the lower O–O frequency of 721 cm^{-1} in $[\{Cu^{II}(MeAN)_2(\mu-\eta^2:\eta^2-O_2^{2-})\}_2]^{2+}$ compared to 765 cm^{-1} for **1** is due to the strong σ donation from the MeAN ligand to Cu. The trans effect from this strong donor ligand decreases the $O_2^{2-} \pi^*$ -to-Cu charge transfer. This results in

more electron density in the π antibonding orbitals of the peroxide and thus the weaker O–O bond. The higher σ donation from the MeAN ligand compared to the ligand system in **1** is consistent with amines (MeAN) being better donors than pyridines (**1**), as reflected by their higher pK_a 's.

An important issue in the binuclear copper(I)/dioxygen study is whether side-on peroxo-dicopper(II) complexes with weak O–O bonds (ν_{O-O} values of 710–730 cm^{-1}) are, in fact, further activated for O–O cleavage compared to those with higher ν_{O-O} (745–765 cm^{-1}). We thus consider whether $[\{Cu^{II}(MeAN)_2(\mu-\eta^2:\eta^2-O_2^{2-})\}_2]^{2+}$ is an intermediate farther along the O–O cleavage coordinate than **1**, converting the side-on peroxo-dicopper(II) to the bis- μ -oxo-dicopper(III) isomer. Along this coordinate, the σ^* on the peroxo is lowered in energy as the O–O bond is elongated, resulting in increased electron donation from Cu^{II} into the peroxo σ^* orbital (backbonding) that leads to the eventual cleavage of the O–O bond (Figure 8). However, from the above analysis, the longer O–O bond in $[\{Cu^{II}(MeAN)_2(O_2^{2-})\}_2]^{2+}$ is not due to an increase in backbonding (Table 7). Thus, $[\{Cu^{II}(MeAN)_2(\mu-\eta^2:\eta^2-O_2^{2-})\}_2]^{2+}$ is not an intermediate in the peroxo to bis- μ -oxo reaction coordinate, and the O–O bond is not further activated for cleavage.

5. CONCLUSION

This study shows that the long O–O bond in $[\{Cu^{II}(MeAN)_2(\mu-\eta^2:\eta^2-O_2^{2-})\}_2]^{2+}$ is stabilized by a strong donor ligand system. Strong donor ligands are also known to stabilize bis- μ -oxo-dicopper(III) species.⁸⁰ Indeed, there is evidence for the presence of a bis- μ -oxo component with the MeAN ligand in different solvents.²⁰ Thus, ligand systems that lead to a bis- μ -oxo component can also lead to a low ν_{O-O} in its side-on peroxo isomer. However, these involve different bonding interactions: a decrease in $O_2^{2-} \sigma$ donation lowers ν_{O-O} , whereas an increase in π backbonding leads to O–O cleavage. The weak O–O bond (721 cm^{-1}) is a result of strong donor ligands, and yet the peroxo moiety is not further activated for cleavage along the side-on peroxo to bis- μ -oxo coordinate compared to side-on peroxo species with stronger O–O bonds (~ 765 cm^{-1}). These results highlight the

importance of understanding the underlying electronic structure in order to correlate spectral changes to reactivity. The results and conclusions derived here should be considered in other cases of copper ion biochemical O₂-binding and activation, and they may well extend to chemical or biochemical systems involving other redox-active metal ions.

■ ASSOCIATED CONTENT

■ Supporting Information

CIF file for the X-ray structure of $[\{\text{Cu}(\text{MeAN})\}_2(\text{O}_2^{2-})]^{2+}$; XANES and EXAFS data and fit for the powder form, XAS edge comparison of paste and powder samples, and XAS edge simulations for quantification of any Cu^I in the paste sample; isosurface plots and Mulliken population of the calculated frontier molecular orbitals of $[\{\text{Cu}(\text{MeAN})\}_2(\text{O}_2^{2-})]^{2+}$ and $[\{\text{Cu}^{\text{II}}(\text{L}_2)\}(\text{O}_2^{2-})]^{2+}$; and optimized Cartesian coordinates of the two peroxo complexes along with charge-transfer contributions calculated from fragment analyses. This material is available free of charge via the Internet at <http://pubs.acs.org>.

■ AUTHOR INFORMATION

Corresponding Author

karlin@jhu.edu

Author Contributions

[†]G.Y.P. and M.F.Q. contributed equally to this work.

Notes

The authors declare no competing financial interest.

■ ACKNOWLEDGMENTS

We are grateful to the NIH (E.I.S., DK31450; K.D.K., GM28962; K.O.H., P41 RR001209) for research support. Portions of this research were carried out at the Stanford Synchrotron Radiation Lightsources, a Directorate of SLAC National Accelerator Laboratory and an Office of Science User Facility operated for the U.S. Department of Energy Office of Science by Stanford University. The SSRL Structural Molecular Biology Program is supported by the DOE Office of Biological and Environmental Research, and by the National Institutes of Health, National Institute of General Medical Sciences (including P41GM103393) and the National Center for Research Resources (P41RR001209). We thank Dr. Jordi Cirera for helpful suggestions with DFT calculations.

■ REFERENCES

- (1) Mirica, L. M.; Ottenwaelder, X.; Stack, T. D. P. *Chem. Rev.* **2004**, *104*, 1013–45.
- (2) Lewis, E. A.; Tolman, W. B. *Chem. Rev.* **2004**, *104*, 1047–76.
- (3) Itoh, S. *Curr. Opin. Chem. Biol.* **2006**, *10*, 115–22.
- (4) Hatcher, L. Q.; Karlin, K. D. *J. Biol. Inorg. Chem.* **2004**, *9*, 669–83.
- (5) Solomon, E. I.; Sundaram, U. M.; Machonkin, T. E. *Chem. Rev.* **1996**, *96*, 2563–605.
- (6) Solomon, E. I.; Chen, P.; Metz, M.; Lee, S. K.; Palmer, A. E. *Angew. Chem., Int. Ed.* **2001**, *40*, 4570–90.
- (7) Kitajima, N.; Fujisawa, K.; Morooka, Y.; Toriumi, K. *J. Am. Chem. Soc.* **1989**, *111*, 8975–6.
- (8) Magnus, K. A.; Hazes, B.; Tonthat, H.; Bonaventura, C.; Bonaventura, J.; Hol, W. G. J. *Proteins* **1994**, *19*, 302–9.
- (9) Hatcher, L. Q.; Karlin, K. D. *Adv. Inorg. Chem.* **2006**, *58*, 131–84.
- (10) Mahadevan, V.; Gebbink, R. J. M. K.; Stack, T. D. P. *Curr. Opin. Chem. Biol.* **2000**, *4*, 228–34.
- (11) Jacobson, R. R.; Tyeklar, Z.; Farooq, A.; Karlin, K. D.; Liu, S.; Zubieta, J. *J. Am. Chem. Soc.* **1988**, *110*, 3690–2.

(12) Karlin, K. D.; Wei, N.; Jung, B.; Kaderli, S.; Zuberbuhler, A. D. *J. Am. Chem. Soc.* **1991**, *113*, 5868–70.

(13) Baldwin, M. J.; Ross, P. K.; Pate, J. E.; Tyeklar, Z.; Karlin, K. D.; Solomon, E. I. *J. Am. Chem. Soc.* **1991**, *113*, 8671–9.

(14) Schatz, M.; Becker, M.; Thaler, F.; Hampel, F.; Schindler, S.; Jacobson, R. R.; Tyeklar, Z.; Murthy, N. N.; Ghosh, P.; Chen, Q.; Zubieta, J.; Karlin, K. D. *Inorg. Chem.* **2001**, *40*, 2312–22.

(15) Zhang, C. X.; Kaderli, S.; Costas, M.; Kim, E.; Neuhold, Y. M.; Karlin, K. D.; Zuberbuhler, A. D. *Inorg. Chem.* **2003**, *42*, 1807–24.

(16) Que, L.; Tolman, W. B. *Angew. Chem., Int. Ed.* **2002**, *41*, 1114–37.

(17) Halfen, J. A.; Mahapatra, S.; Wilkinson, E. C.; Kaderli, S.; Young, V. G.; Que, L.; Zuberbuhler, A. D.; Tolman, W. B. *Science* **1996**, *271*, 1397–400.

(18) Mirica, L. M.; Vance, M.; Rudd, D. J.; Hedman, B.; Hodgson, K. O.; Solomon, E. I.; Stack, T. D. P. *Science* **2005**, *308*, 1890–2.

(19) Op't Holt, B. T.; Vance, M. A.; Mirica, L. M.; Heppner, D. E.; Stack, T. D. P.; Solomon, E. I. *J. Am. Chem. Soc.* **2009**, *131*, 6421–38.

(20) Liang, H.-C.; Zhang, C. X.; Henson, M. J.; Sommer, R. D.; Hatwell, K. R.; Kaderli, S.; Zuberbuhler, A. D.; Rheingold, A. L.; Solomon, E. I.; Karlin, K. D. *J. Am. Chem. Soc.* **2002**, *124*, 4170–1.

(21) The copper(I) complex of 3,3'-iminobis(*N,N'*-dimethylpropylamine) (AN), differing by only one methyl group in its ligand structure compared to MeAN (i.e., –CH₃ for MeAN, –H for AN), reacts with dioxygen in CH₂Cl₂ to instead form a bis- μ -oxo-dicopper(III) species.²⁰

(22) Pidcock, E.; DeBeer, S.; Obias, H. V.; Hedman, B.; Hodgson, K. O.; Karlin, K. D.; Solomon, E. I. *J. Inorg. Biochem.* **1999**, *74*, 1870–8.

(23) Kubas, G. J. *Inorganic syntheses*; Wiley: New York, 1979; Vol. 19.

(24) Tenderholt, A. H. B.; Hodgson, K. O. *PySpline*; Stanford Synchrotron Radiation Laboratory: Stanford, CA, 2006.

(25) George, G. N. *EXAFSPAK*; Stanford Synchrotron Radiation Laboratory: Stanford, CA, 2000.

(26) Rehr, J. J.; Albers, R. C. *Rev. Mod. Phys.* **2000**, *72*, 621–54.

(27) Kodera, M.; Kajita, Y.; Tachi, Y.; Katayama, K.; Kano, K.; Hirota, S.; Fujinami, S.; Suzuki, M. *Angew. Chem., Int. Ed.* **2004**, *43*, 334–7.

(28) Frisch, M. J.; Trucks, G. W.; Schlegel, H. B.; Scuseria, G. E.; Robb, M. A.; Cheeseman, J. R.; Montgomery, J. A., Jr.; Vreven, T.; Kudin, K. N.; Burant, J. C.; Millam, J. M.; Iyengar, S. S.; Tomasi, J.; Barone, V.; Mennucci, B.; Cossi, M.; Scalmani, G.; Rega, N.; Petersson, G. A.; Nakatsuji, H.; Hada, M.; Ehara, M.; Toyota, K.; Fukuda, R.; Hasegawa, J.; Ishida, M.; Nakajima, T.; Honda, Y.; Kitao, O.; Nakai, H.; Klene, M.; Li, X.; Knox, J. E.; Hratchian, H. P.; Cross, J. B.; Bakken, V.; Adamo, C.; Jaramillo, J.; Gomperts, R.; Stratmann, R. E.; Yazyev, O.; Austin, A. J.; Cammi, R.; Pomelli, C.; Ochterski, J. W.; Ayala, P. Y.; Morokuma, K.; Voth, G. A.; Salvador, P.; Dannenberg, J. J.; Zakrzewski, V. G.; Dapprich, S.; Daniels, A. D.; Strain, M. C.; Farkas, O.; Malick, D. K.; Rabuck, A. D.; Raghavachari, K.; Foresman, J. B.; Ortiz, J. V.; Cui, Q.; Baboul, A. G.; Clifford, S.; Cioslowski, J.; Stefanov, B. B.; Liu, G.; Liashenko, A.; Piskorz, P.; Komaromi, I.; Martin, R. L.; Fox, D. J.; Keith, T.; Al-Laham, M. A.; Peng, C. Y.; Nanayakkara, A.; Challacombe, M.; Gill, P. M. W.; Johnson, B.; Chen, W.; Wong, M. W.; Gonzalez, C.; Pople, J. A. *Gaussian 03*, Revision E.01; Gaussian Inc.: Wallingford, CT, 2004.

(29) Becke, A. D. *J. Chem. Phys.* **1993**, *98*, 5648–52.

(30) Becke, A. D. *Phys. Rev. A* **1988**, *38*, 3098.

(31) Lee, C.; Yang, W.; Parr, R. G. *Phys. Rev. B* **1988**, *37*, 785.

(32) Miehlich, B.; Savin, A.; Stoll, H.; Preuss, H. *Chem. Phys. Lett.* **1989**, *157*, 200–6.

(33) Perdew, J. P. *Phys. Rev. B* **1986**, *33*, 8822.

(34) McGrath, M. J. *Chem. Phys.* **1991**, *94*, 511.

(35) Krishnan, R. J. *Chem. Phys.* **1980**, *72*, 650.

(36) Curtiss, L. J. *Chem. Phys.* **1995**, *103*, 6104.

(37) Rassolov, V. J. *Chem. Phys.* **1998**, *109*, 1223.

(38) Hariharan, P. C.; Pople, J. A. *Theor. Chem. Acc.* **1973**, *28*, 213–22.

(39) Francl, M. J. *Chem. Phys.* **1982**, *77*, 3654.

(40) <http://cccbdb.nist.gov/vibscalejust.asp>.

- (41) Schäfer, A. *J. Chem. Phys.* **1994**, *100*, 5829.
- (42) Schäfer, A. *J. Chem. Phys.* **1992**, *97*, 2571.
- (43) Frisch, M. J.; Trucks, G. W.; Schlegel, H. B.; Scuseria, G. E.; Robb, M. A.; Cheeseman, J. R.; Scalmani, G.; Barone, V.; Mennucci, B.; Petersson, G. A.; Nakatsuji, H.; Nakatsuji, H.; Caricato, M.; Li, X.; Hratchian, H. P.; Izmaylov, A. F.; Bloino, J.; Zheng, G.; Sonnenberg, J. L.; Hada, M.; Ehara, M.; Toyota, K.; Fukuda, R.; Hasegawa, J.; Ishida, M.; Nakajima, T.; Honda, Y.; Kitao, O.; Nakai, H.; Vreven, T.; Montgomery, Jr., J. A.; Peralta, J. E.; Ogliaro, F.; Bearpark, M.; Heyd, J. J.; Brothers, E.; Kudin, K. N.; Staroverov, V. N.; Kobayashi, R.; Normand, J.; Raghavachari, K.; Rendell, A.; Burant, J. C.; Iyengar, S. S.; Tomasi, J.; Cossi, M.; Rega, N.; Millam, J. M.; Klene, M.; Knox, J. E.; Cross, J. B.; Bakken, V.; Adamo, C.; Jaramillo, J.; Gomperts, R.; Stratmann, R. E.; Yazyev, O.; Austin, A. J.; Cammi, R.; Pomelli, C.; Ochterski, J. W.; Martin, R. L.; Morokuma, K.; Zakrzewski, V. G.; Voth, G. A.; Salvador, P.; Dannenberg, J. J.; Dapprich, S.; Daniels, A. D.; Farkas, O.; Foresman, J. B.; Ortiz, J. V.; Cioslowski, J.; Fox, D. J. *Gaussian 09*, Revision A.02; Gaussian, Inc.: Wallingford CT, 2009.
- (44) Tenderholt, A. L. *QMForge*, Version 2.1; Stanford University: Stanford, CA, 2007.
- (45) Humphrey, W.; Dalke, A.; Schulten, K. *J. Mol. Graphics* **1996**, *14*, 33–8.
- (46) <http://www.ks.uiuc.edu/Research/vmd/>.
- (47) Addison, A. W.; Rao, T. N.; Reedijk, J.; Vanrijn, J.; Verschoor, G. C. *J. Chem. Soc., Dalton Trans.* **1984**, 1349–56.
- (48) Gubelmann, M.; Williams, A. *Transition Metal Complexes: Structures and Spectra*; Springer-Verlag: Berlin, 1984; pp 1–65.
- (49) Lam, B. M. T.; Halfen, J. A.; Young, V. G.; Hagadorn, J. R.; Holland, P. L.; Lledos, A.; Cucurull-Sanchez, L.; Novoa, J. J.; Alvarez, S.; Tolman, W. B. *Inorg. Chem.* **2000**, *39*, 4059–72.
- (50) Matoba, Y.; Kumagai, T.; Yamamoto, A.; Yoshitsu, H.; Sugiyama, M. *J. Biol. Chem.* **2006**, *281*, 8981–90.
- (51) Ling, J.; Nestor, L. P.; Czernuszewicz, R. S.; Spiro, T. G.; Fraczkiewicz, R.; Sharma, K. D.; Loehr, T. M.; Sanders-Loehr, J. *J. Am. Chem. Soc.* **1994**, *116*, 7682–91.
- (52) Eickman, N. C.; Solomon, E. I.; Larrabee, J. A.; Spiro, T. G.; Lerch, K. *J. Am. Chem. Soc.* **1978**, *100*, 6529–31.
- (53) Chrapkova, J.; Schwendt, P.; Sivak, M.; Repisky, M.; Malkin, V. G.; Marek, J. *Dalton Trans.* **2009**, 465–73.
- (54) John, G. H.; May, I.; Sarsfield, M. J.; Steele, H. M.; Collison, D.; Helliwell, M.; McKinney, J. D. *Dalton Trans.* **2004**, 734–40.
- (55) Charushnikova, I. A.; Den Auwer, C. *Russ. J. Coord. Chem* **2004**, *30*, 511–9.
- (56) Niemeyer, M. Z. *Anorg. Allg. Chem.* **2002**, *628*, 647–57.
- (57) Kondo, S.; Saruhashi, K.; Seki, K.; Matsubara, K.; Miyaji, K.; Kubo, T.; Matsumoto, K.; Katsuki, T. *Angew. Chem., Int. Ed.* **2008**, *47*, 10195–8.
- (58) Falber, A.; Todaro, L.; Goldberg, I.; Favilla, M. V.; Drain, C. M. *Inorg. Chem.* **2007**, *47*, 454–67.
- (59) Masci, B.; Thuéry, P. *Polyhedron* **2005**, *24*, 229–37.
- (60) Tejel, C.; Ciriano, M. A.; Jiménez, S.; Passarelli, V.; López, J. A. *Angew. Chem., Int. Ed.* **2008**, *47*, 2093–6.
- (61) Bradley, D. C.; Ghotra, J. S.; Hart, F. A.; Hursthouse, M. B.; Raithby, P. R. *J. Chem. Soc., Dalton Trans.* **1977**, 1166–72.
- (62) Haegele, R.; Boeyens, J. C. A. *J. Chem. Soc., Dalton Trans.* **1977**, 648–50.
- (63) Karlin, K. D.; Cruse, R. W.; Gultneh, Y.; Farooq, A.; Hayes, J. C.; Zubieta, J. *J. Am. Chem. Soc.* **1987**, *109*, 2668–79.
- (64) Karlin, K. D.; Haka, M. S.; Cruse, R. W.; Meyer, G. J.; Farooq, A.; Gultneh, Y.; Hayes, J. C.; Zubieta, J. *J. Am. Chem. Soc.* **1988**, *110*, 1196–207.
- (65) Shearer, J.; Zhang, C. X.; Zakharov, L. N.; Rheingold, A. L.; Karlin, K. D. *J. Am. Chem. Soc.* **2005**, *127*, 5469–83.
- (66) Zhang, C. X.; Liang, H. C.; Kim, E. I.; Shearer, J.; Helton, M. E.; Kim, E.; Kaderli, S.; Incarvito, C. D.; Zuberbuhler, A. D.; Rheingold, A. L.; Karlin, K. D. *J. Am. Chem. Soc.* **2003**, *125*, 634–5.
- (67) DuBois, J. L.; Mukherjee, P.; Collier, A. M.; Mayer, J. M.; Solomon, E. I.; Hedman, B.; Stack, T. D. P.; Hodgson, K. O. *J. Am. Chem. Soc.* **1997**, *119*, 8578–9.
- (68) Kitajima, N.; Fujisawa, K.; Fujimoto, C.; Morooka, Y.; Hashimoto, S.; Kitagawa, T.; Toriumi, K.; Tatsumi, K.; Nakamura, A. *J. Am. Chem. Soc.* **1992**, *114*, 1277–91.
- (69) Mahapatra, S.; Halfen, J. A.; Wilkinson, E. C.; Pan, G. F.; Wang, X. D.; Young, V. G.; Cramer, C. J.; Que, L.; Tolman, W. B. *J. Am. Chem. Soc.* **1996**, *118*, 11555–74.
- (70) Kau, L. S.; Spirasolomon, D. J.; Pennerhahn, J. E.; Hodgson, K. O.; Solomon, E. I. *J. Am. Chem. Soc.* **1987**, *109*, 6433–42.
- (71) We have previously estimated the minimum detectable limit of a bis- μ -oxo-dicopper(III) isomer in a 4 mM solution of $[\text{Cu}_2(\text{O}_2^{2-})]^{2+}$ to be 0.0005 mM, with the ratio of side-on peroxo to bis- μ -oxo isomer being 1:<0.0013.
- (72) Tolman and co-workers report a non-crystallographically characterized complex $[\{(i\text{Pr}_3\text{tacn})\text{Cu}\}_2(\mu\text{-}\eta^2\text{-}\eta^2\text{-O}_2)]^{2+}$ ($i\text{Pr}_3\text{tacn}$ = 1,4,7-triisopropyl-1,4,7-triazacyclononane), with $\mu\text{-}\eta^2\text{-}\eta^2$ -peroxo-dicopper(II) structure, where $\nu_{\text{O-O}} = 713 \text{ cm}^{-1}$. Holland, P. L.; Cramer, C. J.; Wilkinson, E. C.; Mahapatra, S.; Rodgers, K. R.; Itoh, S.; Taki, M.; Fukuzumi, S.; Que, L., Jr.; Tolman, W. B. *J. Am. Chem. Soc.* **2000**, *122*, 792–802.
- (73) Extension to **2** and **3** reproduces the observed trend in $\nu_{\text{O-O}}$ but not the O–O distances of **2** and **3**. However, the crystal structure of **3** reveals significantly elongated displacement ellipsoids around each oxygen. Moreover, $[\{\text{Cu}^{\text{II}}(\text{MeAN})\}_2(\text{O}_2^{2-})]^{2+}$ is calculated to have the weakest O–O bond compared to **2** and **3**.
- (74) Using the O–O distance and frequency of **1**, Badger's rule predicts the interperoxide stretch in $[\{\text{Cu}^{\text{II}}(\text{MeAN})\}_2(\text{O}_2^{2-})]^{2+}$ to be 704 cm^{-1} , lower than that in **1** by 61 cm^{-1} .
- (75) Calculations with a larger, more saturated basis set (B3, Experimental Section) using B3LYP and BP86 functionals gave an even smaller difference in O–O distance (0.010 Å) and interperoxide vibration (21 cm^{-1}) between the two structures.
- (76) The occupied orbitals spin-polarize and mix. Thus, the unoccupied α - and β -LUMOs are used to quantify the uncompensated spin density involved in bonding.
- (77) The $\text{O}_2^{2-} \pi^* \sigma$ character in the unoccupied orbitals reflects the amount of peroxo-to-Cu charge transfer.
- (78) Ross, P. K.; Solomon, E. I. *J. Am. Chem. Soc.* **1991**, *113*, 3246–59.
- (79) Chen, P.; Fujisawa, K.; Helton, M. E.; Karlin, K. D.; Solomon, E. I. *J. Am. Chem. Soc.* **2003**, *125*, 6394–408.
- (80) Total energy calculations (with B2 basis set) show that the ΔG° associated with the side-on peroxo-dicopper(II) \rightarrow bis- μ -oxo-dicopper(III) isomerization is 10.5 kcal/mol for $\{\text{Cu}^{\text{II}}(\text{MeAN})\}_2(\text{O}_2^{2-})$, compared to 18.8 kcal/mol for **1**, thus showing that stronger donor ligands (amines over pyridines) tend to stabilize bis- μ -oxo-dicopper(III) species.